View metadata, citation and similar papers at core.ac.uk
brought to you by CORE
provided by IntechOpen

We are IntechOpen, the world's leading publisher of Open Access books
Built by scientists, for scientists

4,800
Open access books available

122,000
International authors and editors

135M
Downloads

Our authors are among the

154
Countries delivered to

TOP 1%
most cited scientists

12.2%
Contributors from top 500 universities

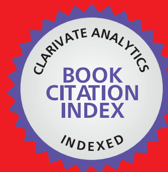

WEB OF SCIENCE™

Selection of our books indexed in the Book Citation Index in Web of Science™ Core Collection (BKCI)

Interested in publishing with us?
Contact book.department@intechopen.com

Numbers displayed above are based on latest data collected.
For more information visit www.intechopen.com

16

Polycrystalline Silicon Piezoresistive Nano Thin Film Technology

Xiaowei Liu[1], Changzhi Shi[1] and Rongyan Chuai[2]
[1]*Harbin Institute of Technology*
[2]*Shenyang University of Technology*
China

1. Introduction

The piezoresistive effect of semiconductor materials was discovered firstly in silicon and germanium (Smith, 1954). Dissimilar to the piezoresistive effect of metal materials induced from the change in geometric dimension, the piezoresistive phenomenon in silicon is due to that mechanical stress influences the energy band structure, thereby varying the carrier effective mass, the mobility and the conductivity (Herring, 1955). The gauge factor (GF) is used to characterize the piezoresistive sensitivity and defined as the ratio of the relative resistance change and the generated strain (nondimensional factor). Usually, the GF in silicon is around 100 and changes with stress direction, crystal orientation, doping concentration, etc. Recently, the giant piezoresistances were observed in silicon nanowires (He & Yang, 2006; Rowe, 2008) and metal-silicon hybrid structures (Rowe, et al., 2008), respectively. Although these homogeneous silicon based materials or structures possess high piezoresistive sensitivity, there are still several issues influencing their sensor applications, such as, p-n junction isolation, high temperature instability, high production cost and complex fabrication technologies.

As another monatomic silicon material with unique microstructure, polycrystalline silicon has been investigated since the 1960s. The discovery of its piezoresistive effect (Onuma & Sekiya, 1974) built up a milestone that this material could be applied widely in field of sensors and MEMS devices. Moreover, polycrystalline silicon could be grown on various substrate materials by physical or chemical methods, which avoids p-n junction isolation and promotes further its applications for piezoresistive devices (Jaffe, 1983; Luder, 1986; Malhaire & Barbier, 2003). Among numerous preparation methods, the most popular technology is chemical vapour deposition (CVD), which includes APCVD, LPCVD, PECVD, etc. The PECVD method can deposit films on substrates at lower temperatures, but the stability and uniformity of as-deposited films are not good, and the samples could contain a large number of amorphous contents. Subsequently, the metal-induced lateral crystallization (MILC) technique was presented (Wang, et al., 2001). By enlarging grain size and improving crystallinity, the gauge factor of MILC polycrystalline silicon was increased to be about 60. But the MILC polycrystalline silicon-based devices could suffer the contamination from the metal catalyst layer (e.g. Ni, Al, etc.). Compared with the aforementioned technologies, the LPCVD process is a mature and stable CVD method with

Source: Solid State Circuits Technologies, Book edited by: Jacobus W. Swart,
ISBN 978-953-307-045-2, pp. 462, January 2010, INTECH, Croatia, downloaded from SCIYO.COM

advantages of good product uniformity, low cost, IC process compatibility, etc. Therefore, the preparation method in this work is mainly based on LPCVD, while the magnetron sputtering technology will be utilized as a reference result.

The experimental results reported by other researchers indicate that the gauge factor of polycrystalline silicon thicker films (around 400nm in thickness generally) has a maximum as the doping concentration is at the level of 10^{19} cm^{-3} and then degrades rapidly with the further increase of doping concentration (Schubert, et al., 1987; French & Evens, 1989; Gridchin, et al., 1995; Le Berre, et al., 1996). Moreover, the gauge factor of highly doped polycrystalline silicon thicker films is only 20-25. It results in that the research works were emphasized on the medium doped polycrystalline silicon thicker films. However, the lower doping concentration brings the higher temperature coefficients of resistance and gauge factor. This limits the working temperature range of polycrystalline silicon thicker film-based sensors.

In our research work, when the film thickness is reduced to nanoscale and the doping concentration is elevated to the level of 10^{20} cm^{-3}, the enhanced piezoresistance effect is observed, and the temperature coefficients of resistance and gauge factor are reduced further. These phenomena are different from the polycrystalline silicon thicker films and can not be explained reasonably based on the existing piezoresistive theory. The unique properties of polycrystalline silicon nano thin films (PSNFs) could be useful for the design and fabrication of piezoresistive sensors with miniature volume, high sensitivity, good temperature stability and low cost. In the following sections, the details of sample fabrication, microstructure characterization, experimental method and measurement results will be provided. In order to analyze the experimental results, the tunnelling piezoresistive theory is established and predicts the experimental results with a good agreement.

2. Film preparation technologies

2.1 Low pressure chemical vapor deposition

Due to the aforementioned advantages, the low pressure chemical vapour deposition (LPCVD) technology is utilized to prepare the polycrystalline silicon films. According to the difference of technological parameters, three groups of film samples were prepared (Group A — different thicknesses; Group B — different doping concentrations; Group C — different deposition temperatures).

a. Group A — Firstly, by controlling deposition time, the polycrystalline silicon thin films with different thicknesses were deposited on 500 μm-thick (100) and (111) silicon substrates (4 inch diameter) coated with 1μm-thick thermally grown SiO_2 layers by LPCVD at 620 °C at 45~55 Pa, respectively. For the (100) substrates, the thicknesses of as-deposited films are in the range of 30~90 nm; for the (111) substrates, the film thicknesses are ranged from 123 nm to 251 nm. Then, the solid-state boron diffusion was performed at 1080 °C in N_2 atmosphere with a flow rate of 2L/min to obtain the doping concentration of 2.3×10^{20} cm^{-3}.

b. Group B — Subsequently, according to the piezoresistive sensitivities of polysilicon thin films with different thicknesses, the optimal film thickness was extracted. The experimental results show that the ~80 nm-thick films possess the highest gauge factor (discussed later). Therefore, the thickness of polysilicon thin films with different doping concentrations was selected to be 80 nm. After the same LPCVD process, the obtained polysilicon thin films were ion-implanted by boron dopants with doses of

9.4×10^{13}~8.2×10^{15} cm^{-2}. Then, the post-implantation annealings were carried out in N_2 at 1080 °C for 30 min to activate dopants and eliminate ion-implantation damages. Finally, the doping concentrations were in the range of 8.1×10^{18} ~ 7.1×10^{20} cm^{-3}.

c. Group C — Before preparing films, a 1 μm-thick SiO_2 layer was grown on the 500 μm-thick (111) Si wafers (4 inch diameter) by thermal oxidization at 1100 °C. Then, the 80 nm-thick PSNFs were deposited on the thermally oxidized Si substrates by LPCVD at a pressure of 45~55 Pa over a temperature range of 560~670 °C. The reactant gas was SiH_4 and the flow rate was 50 mL/min. Since the films deposited at 560~600 °C exhibited amorphous appearance mixed with polycrystals, the pre-annealing was performed on them in dry N_2 at 950° C for 30 min to induce the recrystallization of amorphous regions. For the dopant implantation, boron ions were implanted into the samples at a dose of 2×10^{15} cm^{-2} at 20 keV. For the sake of dopant activation and ion implantation damage elimination, the post-implantation annealing was carried out in N_2 atmosphere at 1080 °C for 30 min. Then, the doping concentration was estimated to be 2×10^{20} cm^{-3}.

2.2 Magnetron sputtering

As a reference, a group of samples were prepared by magnetron sputtering. Before preparing films, a 1 μm-thick SiO_2 layer was grown on the 500 μm-thick (100) Si wafers (4 inch diameter) by thermal oxidization at 1100 °C. Then, the polycrystalline silicon films were prepared by magnetron sputtering system from an undoped silicon target and the substrate temperature was 300 °C. The base pressure of system was maintained at 0.12 Pa. The discharge current on the magnetron was held constant at 0.3 A, while the substrate bias voltage was 500 V. The sputtering time was 10 min, and the thickness of films was 200 nm. Through the SEM observation, it can be seen that the obtained films are amorphous. Thus, the annealing of 1080 °C was carried out in N_2 atmosphere for 60 min to obtain the lowest film resistivity. After annealing, the solid-state boron diffusion was performed at 1080 °C in N_2 with a flow rate of 2 L/min to obtain the doping concentration of 2.3×10^{20} cm^{-3}.

3. Microstructure characterization

3.1 Samples with different thicknesses

In order to analyze the surface morphology, the film samples with different thicknesses were characterized by SEM. The SEM images of samples with different thicknesses are given in Fig. 1. For the characterization of grain orientation, the XRD experiment was performed. The XRD patterns of samples with different thicknesses are shown in Fig. 2. From the SEM images in Fig. 1, it can be seen that the grain size of the samples increases with increasing film thickness. For 30, 40, 60, 90, 123, 150, 198, 251 nm-thick samples, their grain sizes are 11, 30, 37, 48, 48, 58, 69, 80 nm, respectively. By XRD analysis, the (111) peaks of the films thicker than 120 nm and the (400) peaks of the films thinner than 100 nm are attributed to the crystal orientation of substrates. It can be also observed that the (220), (400) and (331) peaks appear as the films are thicker than 120 nm and the intensities of these diffract peaks increase with the increase of film thickness. Moreover, the (311) peak is observed in 251 nm-thick films. It indicates that the increase in film thickness improves the crystallinity and enhances the preferred growth. However, no obvious diffract peaks are observed in 60 and 90 nm-thick films, so they could be considered to be randomly oriented. Noticeably, the (201) peaks appear in 30 and 40 nm-thick samples. According to the report (Zhao et al., 2004), this preferred orientation occurs in nanocrystalline silicon and corresponds to

tetragon microstructure. It indicates that these two samples exhibit the structural characteristic of nanocrystalline silicon. For the sake of brevity, the 60-100 nm-thick films are called polysilicon nano thin films (PSNFs), while the films thicker than 120 nm are called polysilicon common films (PSCFs). The films thinner than 50 nm are called nanocrystalline-like polysilicon thin films (NL-PSTFs).

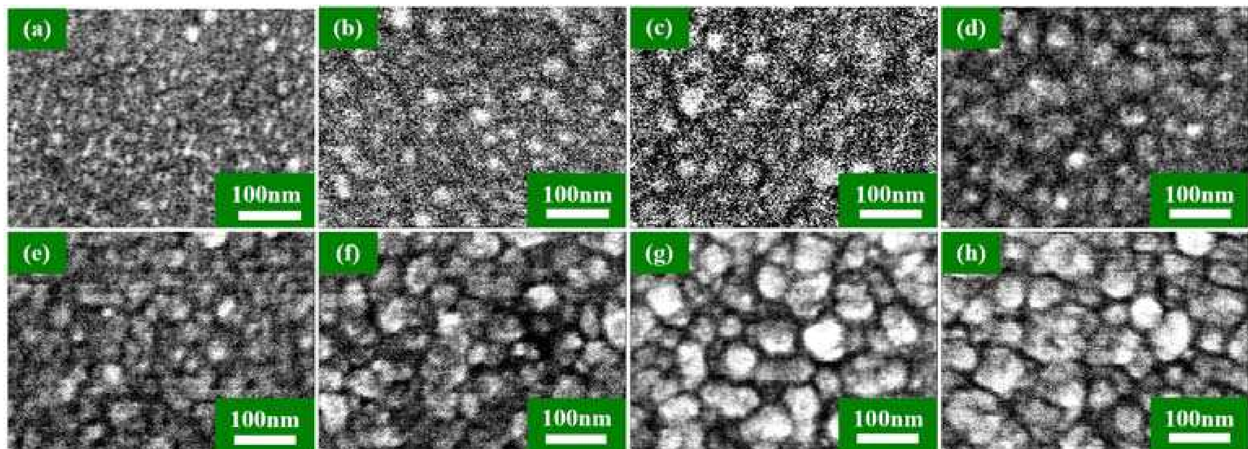

Fig. 1. SEM images of polycrystalline silicon thin film samples with different thicknesses

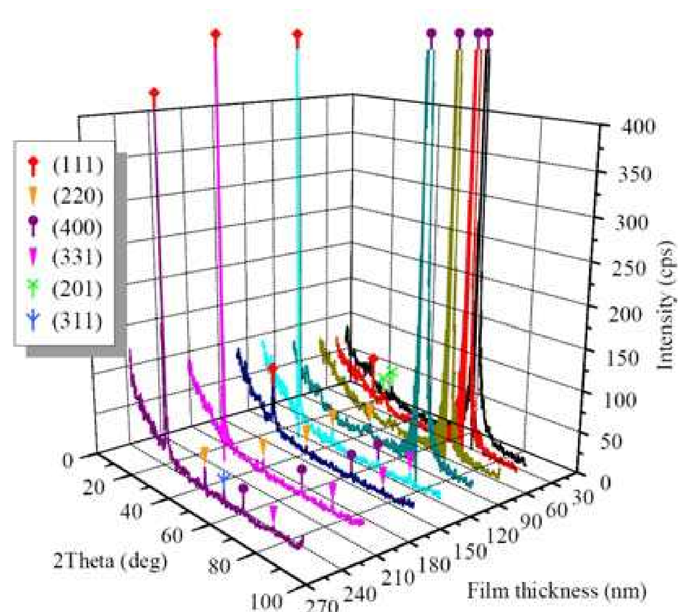

Fig. 2. XRD patterns of polycrystalline silicon thin films with different thicknesses

3.2 Samples with different doping concentrations

Fig. 3 provides the SEM and TEM images of the 80 nm-thick PSNFs with doping concentrations of 2×10^{19} cm^{-3}, 4.1×10^{19} cm^{-3} and 4.1×10^{20} cm^{-3}. It can be observed that the variation of doping concentration does not influence the grain size obviously. Thus, the grain size of the samples with different doping concentrations is considered to be constant. In the XRD pattern of Fig. 4, only the weak (220) peak is observed and the strong (111) peak is attributed to the crystal orientation of substrates. It indicates that these samples are randomly oriented.

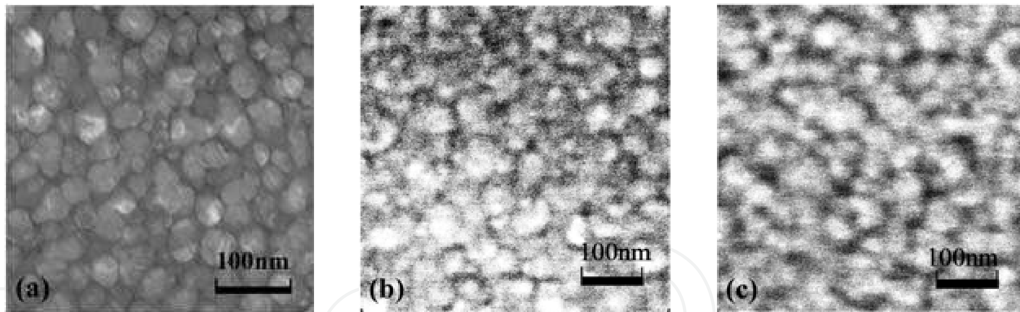

Fig. 3. TEM and SEM images of 80 nm-thick PSNF samples with different doping concentrations. (a) 2×10^{19} cm^{-3} TEM; (b) 4.1×10^{19} cm^{-3} SEM; (c) 4.1×10^{20} cm^{-3} SEM

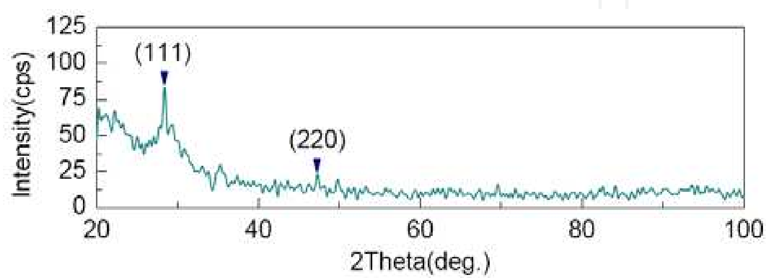

Fig. 4. XRD spectrum of 80 nm-thick polycrystalline silicon nano thin films

3.3 Samples with different deposition temperatures

The surface morphology of PSNFs was characterized by SEM, as shown in Figs. 5(a)-(e). It can be seen that the grain size increases with elevating deposition temperature. This indicates that the crystallinity of PSNFs can be improved by raising deposition temperature. The grain size can be determined by TEM, as shown in Fig. 5(f). The mean grain size of 620 °C samples is estimated to be 40 nm approximately. With the deposition temperature varying from 560 °C to 670 °C, the mean grain size increases from 30 nm to 70 nm. For the sake of clarity, the 560~600 °C films undergoing the preannealing of 950 °C are called

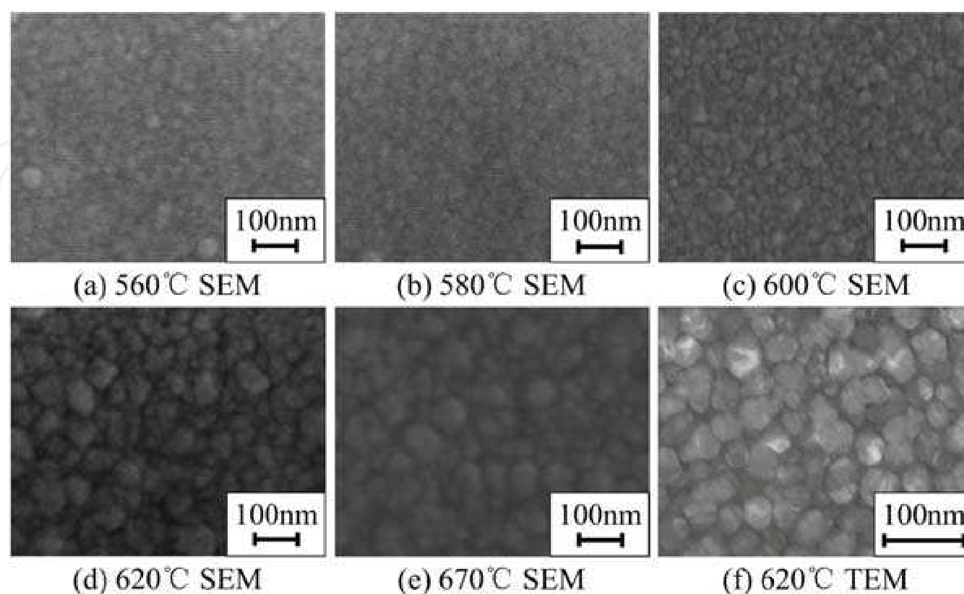

Fig. 5. SEM and TEM images of PSNFs deposited at different temperatures

recrystallized (RC) PSNFs, while the 620~670 °C films are called directly crystallized (DC) PSNFs. From Fig. 5, it can be seen that the borders between grain boundaries and grains of RC PSNFs are obscure as well as the 670 °C samples. It shows that the grain boundaries of the abovementioned samples contain a large number of amorphous phases.

In order to analyze the film microstructure, the XRD experiment was performed on the samples. In the XRD spectra shown in Fig. 6, all the (111) peaks are attributed to Si substrates. The clear (220) peak of 670 °C PSNFs is due to the preferred grain growth along (220) orientation, while the other PSNFs are oriented randomly. Furthermore, it should be noted that the broad peaks (2θ=85~100 °) related to amorphous phases appear on the spectra of RC and 670 °C PSNFs, thereby testifying the existence of amorphous phases at grain boundaries. Because amorphous phases in the 620 °C PSNFs are much fewer, no remarkable broad peak is observed. The peak intensity and FWHM of RC PSNFs are larger than those of the 670 °C ones. It demonstrates that the crystallinity of RC PSNFs is lower than DC ones. The broad peak of 670 °C samples is likely due to the preferred growth aggravating disordered states of grain boundaries.

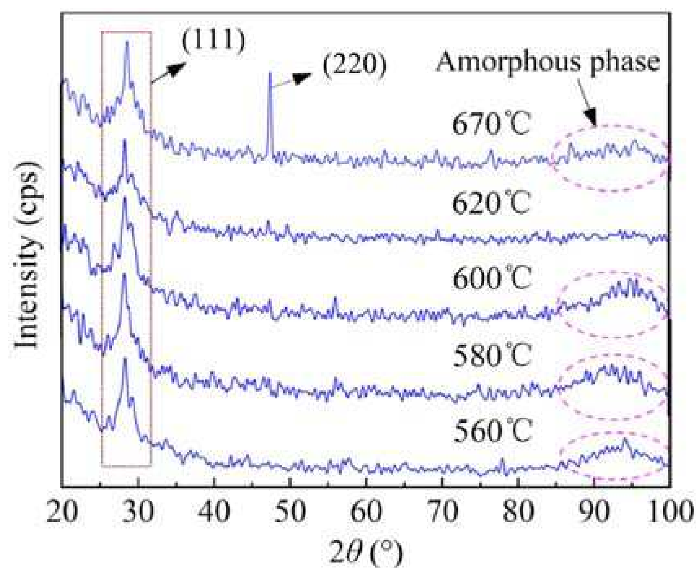

Fig. 6. XRD spectra of PSNF samples deposited at different temperatures

3.4 Magnetron sputtering samples

Fig. 7 provides the SEM images of polycrystalline silicon films prepared by magnetron sputtering before and after the annealing of 1080 °C. From Fig. 7(a), we can see that the film is amorphous and has no micrograined texture. After high temperature annealing, the

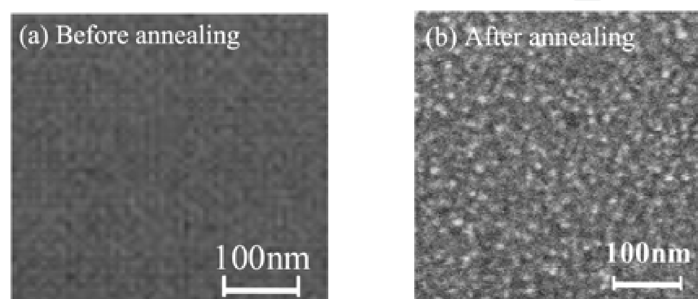

Fig. 7. SEM images of polycrystalline silicon films prepared by magnetron sputtering

recrystallization occurs in the film, which make the film transfer from amorphous state to polycrystalline state, as shown in Fig. 7(b). By calculation, the grain size of magnetron sputtering films is around 10 nm. It indicates that the crystallinity of magnetron sputtering films is very low and the recrystallization induced by high temperature annealing is limited for the improvement of film crystallinity.

4. Fabrication of cantilever beam samples

4.1 Piezoresistors

For measuring gauge factor, the cantilever beams were fabricated based on photolithography and etching technologies. Firstly, the sample wafers were ultrasonically degreased with methylbenzene, acetone and ethanol for 5 min in each and then rinsed repeatedly in de-ionized water. The cleaned samples were pre-baked at 120 °C for 15 min. Next, after spin-coating with positive photoresist and a soft-bake at 90°C for 10 min, the samples were exposed for 90 s using the mask plate as shown in Fig. 8(a) and developed in the 0.5% NaOH solution. Then, a hard-bake for 25 min was performed at 120 °C for the successive etching process. After photolithography, the samples were etched in HNO_3/HAc/HF (4:1:1) solution to form PSNF resistors and then rinsed in de-ionized water. The photoresist was removed by acetone to obtain the sample wafers with PSNF resistors as shown in Fig. 8(b).

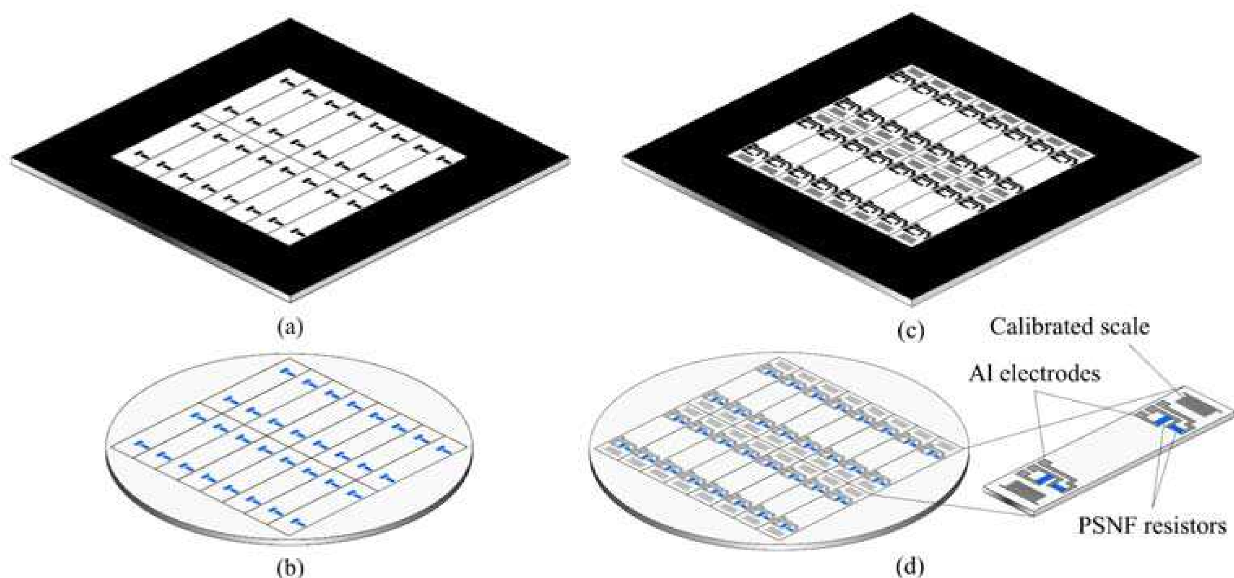

Fig. 8. Schematic diagram of mask plates and sample wafers in the fabrication of cantilever beams. (a) The mask plate for patterning resistors. (b) The sample wafer after patterning resistors. (c) The mask plate for patterning electrodes and calibrated scales. (d) The sample wafer and the cantilever beam after fabricating electrodes and calibrated scales.

4.2 Metal contact electrodes

Here, the aluminium is used as the metal electrode material. In order to measure the contact resistance between PSNFs and metal electrodes, the ohmic contact test patterns based on linear transmission line model (LTLM) were also fabricated on the samples. Before depositing metal, the samples were dipped in HF/H_2O (1:10) for 8 s to remove the native

oxide. The Al layer was evaporated onto the samples by vacuum evaporation. Then, the positive photoresist was coated and patterned in the same process as the resistor fabrication. The schematic diagram of mask plate is shown in Fig. 8(c). The Al layer was etched in concentrated phosphorous acid at 80~100 °C to form electrodes. The electrode fabrication was completed by removing the photoresist left.

4.3 Alloying and scribing

After scribing, the sample wafers were divided into individual cantilever beams of 26 mm×4 mm, as shown in Fig. 8(d). Then, the samples were alloyed at 410 °C, 450 °C and 490 °C for 20 min in N_2 to form ohmic contact. By measuring the LTLM test patterns, the *I-V* characteristic curves after alloying at different temperatures are provided in Fig. 9. From Fig. 9, it can be seen that the samples annealed at 450 °C have a linear *I-V* curve, which indicates that the good ohmic contact is formed. The specific contact resistivity is about 2.4×10^{-3} Ω·cm^2.

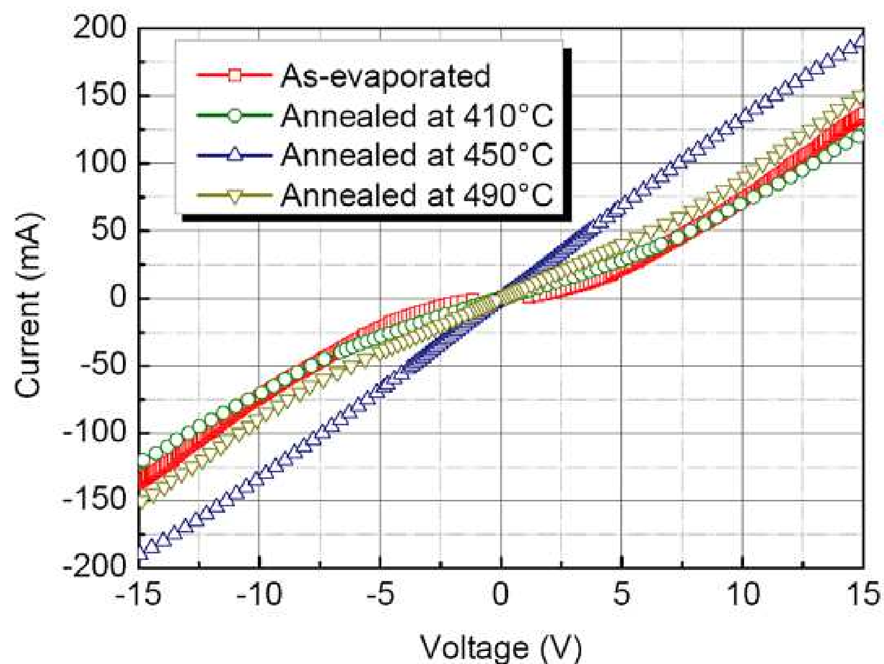

Fig. 9. *I-V* characteristic curves of metal contact electrodes after annealed at different alloying temperatures

Finally, on the actual cantilever beam sample given in Fig. 10, two groups of PSNF piezoresistors were fabricated. Each group consists of three sets of longitudinal and transversal piezoresistors with length-width ratios of 1:4, 2:1 and 8:1, respectively. And the current directions through longitudinal resistors were aligned with the (110) orientation. Fig. 10(b) and (c) are the micrographs of a PSNF resistor taken by laser scanning microscope. Also, the Al calibrated scales were fabricated near both ends of cantilever beams for measuring the arm of applied force.

5. Gauge factor measurement

The gauge factor test setup is shown in Fig. 11. Either end of the cantilever beam is fixed by the clamp. The piezoresistors are connected to the electric instruments through Al electrodes.

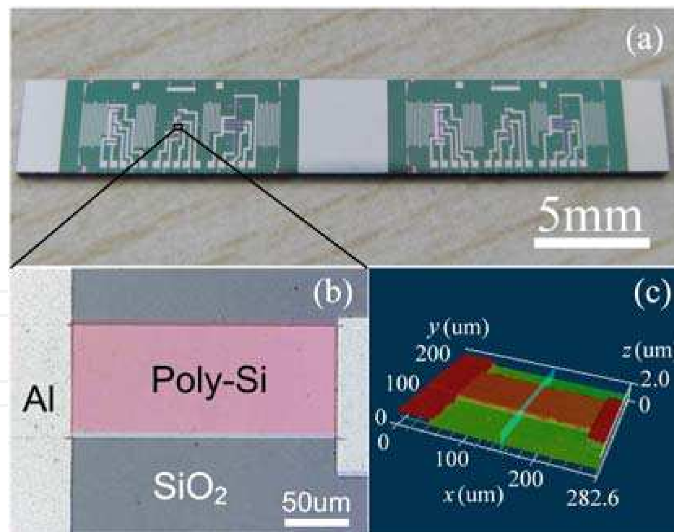

Fig. 10. (a) Photo of a cantilever beam sample; (b) Laser scanning microscope 2D image of a polysilicon piezoresistor; (c) Laser scanning microscope 3D image of a polysilicon piezoresistor

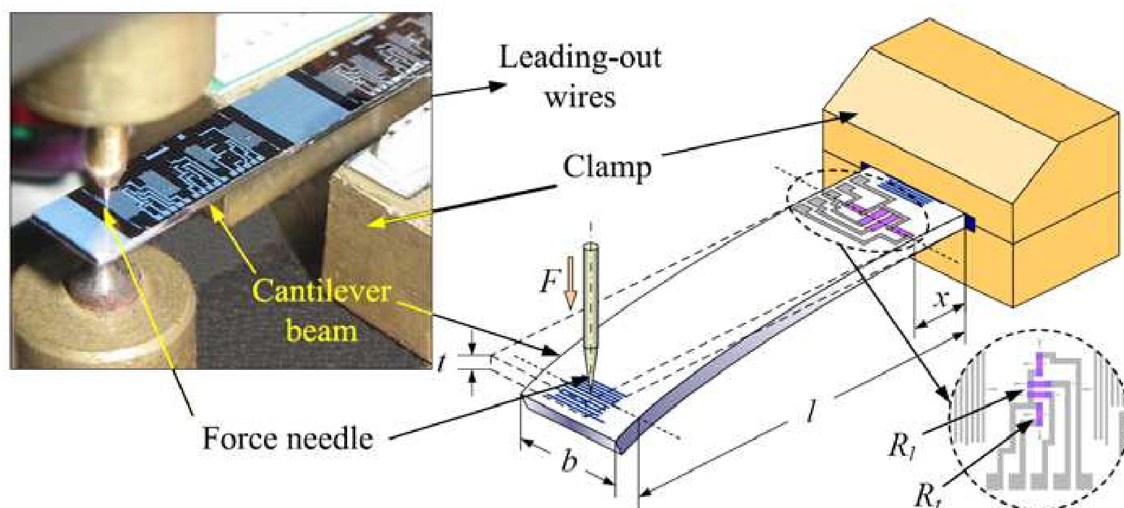

Fig. 11. Strain loading setup for measuring gauge factor

When an axial force F is applied to the free end of the cantilever beam, the strain $\varepsilon(x)$ produced at x can be expressed as

$$\varepsilon(x) = \frac{6(l-x)\cdot F}{bt^2Y} \tag{1}$$

where l is the force arm of the axial force F, b and t are the width and the thickness of the cantilever beam (b, t << l here), respectively. Y is Young's modulus of silicon. The initial resistance R_0 (without strain) and the varied resistance R (with strain) were measured by a Keithley 2000 digital multimeter. The gauge factor can be calculated by:

$$GF = \frac{R-R_0}{R_0\cdot\varepsilon} = \frac{\Delta R}{R_0\cdot\varepsilon} \tag{2}$$

6. Tunneling piezoresistive theory

6.1 Analysis of existing theories

The existing piezoresistive theories of polysilicon were established during 1980s~1990s and used to ameliorate the process steps for the optimization of device performance. In the early models proposed (Mikoshiba, 1981; Erskine, 1983; Germer & Tödt, 1983), the contribution of grain boundaries to piezoresistive effect was neglected, thereby resulting in the discrepancy between experimental data and theoretical results at low doping levels. To tackle this issue, Schubert et al. took the piezoresistive effect of depletion region barriers (DRBs) arising from carrier trapping at grain boundaries into account and established a theoretical model for calculating gauge factors (Schubert, et al., 1987). Thereafter, French et al. suggested that the piezoresistive effect of p-type polysilicon is not only due to the shift in heavy and light hole band minima relative to each other, but also due to the warpage of two sub-bands (French & Evens, 1989). Moreover, the barrier effect of grain boundaries was introduced into the model, achieving the good agreement with the experimental data. Noticeably, it was considered in these models that the PRCs of grain boundaries and DRBs are much lower than that of grain neutral regions. Based on this viewpoint, since the PRC of grain neutral regions (bulk Si) falls off rapidly at high doping concentrations (Toriyama & Sugiyama, 2002), it has been considered that the gauge factor of polysilicon could be degraded sharply with increasing doping concentrations. Accordingly, the optimization of fabrication technologies was emphasized on improving crystallinity and controlling doping concentration to prepare the films with larger grain sizes and lower trap densities. It results in that the research works have been mainly focused on polycrystalline silicon thicker films and scarcely involving PSNFs.

6.2 Carrier transport mechanisms through grain boundaries

Polysilicon can be considered as composed of small crystals joined together by grain boundaries. Each crystal is viewed as a Si single crystal, while the grain boundaries are full of defects and dangling bonds and form extremely thin amorphous layers. The forbidden band width of grain boundaries is larger than that of monocrystalline silicon (1.12 eV) (Mandurah, et al., 1981; Kamins, 1971) and approaches that of amorphous silicon (1.5-1.6 eV) (Taniguchi, et al., 1978). The Fermi level is pinned near the midgap at grain boundaries. In this case, the grain boundary barriers are formed to hinder carriers from traversing grain boundaries. Moreover, dangling bonds at grain boundaries can be occupied by carriers and dopant atoms, so the DRBs are created on the sides of grain boundaries. As a result, the grain boundary barriers and the DRBs form the composite grain boundary barriers.

Theoretically, carriers pass through grain boundaries by two transport mechanisms of thermionic emission and tunneling. For simplification, the carrier transport is considered to be one-dimensional. So, according to the kinetic energy E_x of carriers, there are three current components in the conduction current of carriers traversing grain boundaries (Fig. 12), where w, δ, $q\phi$ and qV_b are the DRB width, the grain boundary width, the grain boundary barrier height and the DRB height, respectively. At very low temperatures, $E_x<qV_b$, carriers traverse the composite grain boundaries only by tunneling, forming the field emission current J_1; At intermediate temperatures, $qV_b<E_x<q\phi$, carriers cross the DRBs by thermionic emission and penetrate the grain boundary barrier by tunneling, forming the composite current J_2; At very high temperatures, $E_x>q\phi$, carriers traverse the composite grain boundary completely by thermionic emission, forming the thermionic emission current J_3. In the temperature range of polysilicon devices working, J_2 is dominant, and J_1 and J_3 could be neglected (Mandurah, et al., 1981).

In our tunneling piezoresistive model, the piezoresistive effect of grain boundaries is due to that the stress induced deformation gives rise to the split-off of the degenerate heavy and light hole sub-bands, thereby causing the carrier transfer between two bands and the conduction mass shift. Inside each grain, due to the single crystal nature of grain neutral regions, the gauge factor of this regions, GF_g, is dependent on the PRC of Si single crystals, π_g. The gauge factor of composite grain boundaries, GF_b, is dependent on the PRC of DRBs (π_d) and the PRC of grain boundary barriers (π_δ). Hence, in order to explain the piezoresistive behavior of PSNFs theoretically, it is necessary to deduce the relationship between π_g, π_d and π_δ.

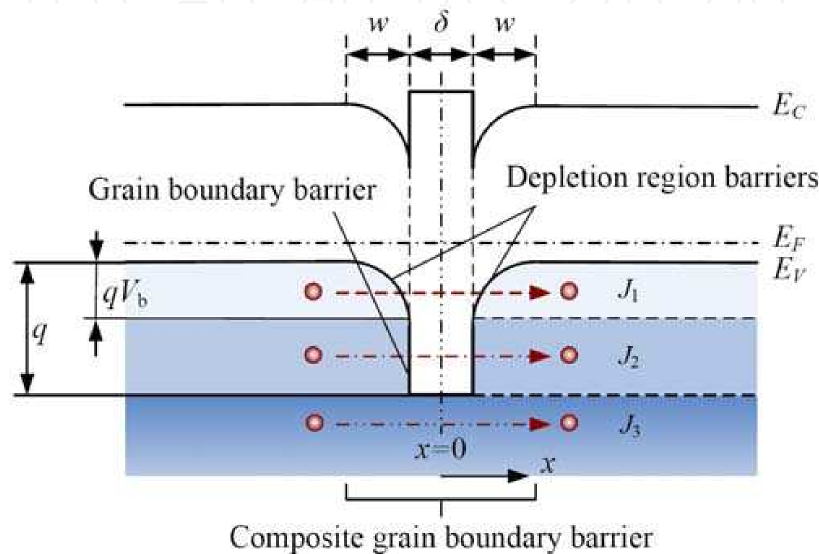

Fig. 12. Energy band structure and carrier transport mechanisms near grain boundaries

6.3 Tunneling current through grain boundary barriers

For DRBs, based on the dependence of thermionic emission current on strain, the relational expressions of longitudinal PRC π_{dl} and transversal PRC π_{dt} in the <111> orientation have been derived in our previous work (Liu, et al., 2004) and expressed as:

$$\pi_{dl} = 0.525\,\pi_{gl} \tag{4}$$

$$\pi_{dt} = 0.616\,\pi_{gt} \tag{5}$$

where π_{gl} and π_{gt} are the longitudinal and transversal PRCs of p-type monocrystalline silicon in the <111> orientation, respectively.

Before deducing the PRC π_δ, the conduction current of carriers penetrating grain boundary barriers must be determined. Fig. 13 provides the energy band diagram and tunneling mechanism of grain boundary barrier omitting DRBs. It is assumed that the voltage drop over the grain boundary barrier is V_δ. Using Fermi-Dirac statistics, the number of holes having energy within the range dE_x incident from left to right on the grain boundary barrier per unit time per unit area is (Murphy & Good, 1956):

$$N(T,\xi,E_x)dE_x = \frac{4\pi \cdot m_d kT}{h^3}\ln\left\{1+\exp\left[\frac{-(E_x+\xi)}{kT}\right]\right\}dE_x \tag{6}$$

where m_d is the effective mass of holes for state density, $\xi = E_F - E_V$, is the difference of Fermi level and valence band edge, h is Planck's constant, k is Boltzmann's constant, T is the absolute temperature.

Fig. 13. Energy band diagram and tunneling mechanism of grain boundary barrier omitting depletion region barriers.

The grain boundary width δ is very small (around 1nm), and the number of the holes with high energies around $q\phi$ is few. Hence, when calculating the current density, the oblique distribution of energy band at the top of grain boundary barrier in Fig. 13 can be substituted by the horizontal line approximately. So, the probability of carriers with the energy E_x ($0 \le E_x \le q\phi - qV_\delta / 2$) tunneling the GB barrier is given by:

$$D(E_x) = \exp\left\{\frac{-4\pi\delta}{h}\left[2m_i(a - E_x)\right]^{1/2}\right\} \tag{7}$$

$$a = q\phi - \frac{1}{2}qV_\delta \tag{8}$$

where m_i is the hole effective mass in the tunneling direction. In Fig. 13, the left valence band edge E_{VL} is taken to be the zero point of energy. By deducing from Eqs. (6)-(8), the current density of holes tunneling grain boundary barrier from left to right is:

$$S_{LR} = \int_0^a N(T,\xi,E_x)\cdot D(E_x)dE_x \tag{9}$$

The current density of holes tunneling grain boundary barrier from right to left is:

$$S_{RL} = \int_0^a N(T,\xi',E_x)\cdot D(E_x)dE_x \tag{10}$$

$$\xi' = \xi + qV_\delta \tag{11}$$

By simplifying the logarithmic function term in Eq. (6) into the exponential form, Eq. (9) can be expressed as:

$$S_{LR} = \frac{4\pi\cdot m_d kT}{h^3}\int_0^a \exp\left[\frac{-(E_x+\xi)}{kT}\right]\cdot D(E_x)dE_x\,. \tag{12}$$

Considering the fact that the holes gather mostly near the valence band edge, when solving the integration in Eq. (12), the square root term is expended by the Taylor's series as follows:

$$\left(a-E_x\right)^{1/2}=\sqrt{a}-\frac{E_x}{2\sqrt{a}}+\cdots. \tag{13}$$

Substituting Eq. (13) into Eq. (7), Eq. (12) can be solved out by integrating:

$$S_{LR}=\frac{4\pi m_d k^2T^2}{h^3c_1}\left[\exp\left(-\frac{2\pi\delta}{h}\sqrt{2m_ia}-\frac{a+\xi}{kT}\right)-\exp\left(-\frac{4\pi\delta}{h}\sqrt{2m_ia}-\frac{\xi}{kT}\right)\right], \tag{14}$$

where

$$c_1=\frac{2\pi\delta}{h}kT\sqrt{\frac{2m_i}{a}}-1. \tag{15}$$

Similarly,

$$S_{RL}=\frac{4\pi m_d k^2T^2}{h^3c_1}\left[\exp\left(-\frac{2\pi\delta}{h}\sqrt{2m_ia}-\frac{a+\xi'}{kT}\right)-\exp\left(-\frac{4\pi\delta}{h}\sqrt{2m_ia}-\frac{\xi'}{kT}\right)\right]. \tag{16}$$

Then, the current density of tunneling boundary barrier region can be given by:

$$\begin{aligned}J_\delta&=q(S_{LR}-S_{RL})\\&=q\frac{4\pi m_d k^2T^2}{h^3c_1}\exp\left(-\frac{\xi}{kT}\right)\cdot\left[\exp\left(c_2-\frac{a}{kT}\right)-\exp\left(c_2-\frac{a+qV_\delta}{kT}\right)-\exp\left(2c_2\right)+\exp\left(2c_2-\frac{qV_\delta}{kT}\right)\right],\end{aligned} \tag{17}$$

where

$$c_2=-\frac{2\pi\delta}{h}\sqrt{2m_ia}. \tag{18}$$

In the case of low voltage bias ($qV_\delta << kT$), the exponential terms in Eq. (17) can be expanded by using the Taylor's series. After taking the first order approximation, it yields:

$$J_\delta=\frac{4\pi q^2 m_d kT}{h^3c_1}\exp\left(-\frac{\xi_p}{kT}\right)\cdot\left[\exp\left(c_2-\frac{a}{kT}\right)-\exp\left(2c_2\right)\right]\cdot V_\delta. \tag{19}$$

Considering the hole concentration formula:

$$p=N_V\exp\left(\frac{-\xi}{kT}\right)=2\left(\frac{2\pi m_d kT}{h^2}\right)^{\frac{3}{2}}\exp\left(\frac{E_V-E_F}{kT}\right), \tag{20}$$

and then Eq. (19) can be rewritten as:

$$J_\delta=\frac{pq}{c_1}\left(\frac{kT}{2\pi m_d}\right)^{1/2}\left[\exp\left(c_2-\frac{a}{kT}\right)-\exp\left(2c_2\right)\right]\cdot\frac{qV_\delta}{kT}=pJ_{\delta 0}. \tag{21}$$

When two sub-bands split off under an axial stress, the total tunneling current (J_δ) consists of tunneling currents of heavy holes ($J_{\delta 1}$) and light holes ($J_{\delta 2}$) and can be expressed as:

$$J_\delta = \sum_{j=1}^{2} J_{\delta j} = J_{\delta 1} + J_{\delta 2}, \quad (22)$$

$$J_{\delta j} = p_j \left(J_{\delta 0}\right)_j, \quad (23)$$

where $J_{\delta j}$ is the tunneling current component of degenerate sub-band, p_j is the corresponding hole concentration, the subscript j=1, 2, represents the heavy and light hole sub-bands, respectively.

6.4 Piezoresistance coefficient of grain boundary barriers

When the heavy and light hole sub-bands split off under stress, the band shift ε′ is defined as the shift of two split-off sub-bands (E_{V1} and E_{V2}) relative to the initial degenerate band (E_V). For the sake of simplification, the applied axial stress is assumed to be along the <111> orientation. According to the result of the cyclotron resonance experiment (Hensel & Feher, 1963), the effective mass of holes under an axial stress is obtained in Table 1, where m_{lj} and m_{tj} are the longitudinal and transversal effective mass of holes at the sub-band E_{Vj}, respectively.

m_{l1}	m_{t1}	m_{d1}	m_{l2}	m_{t2}	m_{d2}
0.870	0.170	0.293	0.135	0.369	0.264

Table 1. Hole effective mass in highly stressed silicon (unit: free-electron mass m_0)

The split-off heavy and light hole sub-bands are $E_V+\varepsilon'$ and $E_V-\varepsilon'$, respectively. By differentiating Eq. (20) and substituting dE_V by the band shift ε', the concentration changes of two sorts of holes are, respectively:

$$\Delta p_1 = N_{v1} \exp\left(\frac{E_V - E_F}{kT}\right) \cdot \frac{\varepsilon'}{kT}, \quad (24)$$

$$\Delta p_2 = -N_{v2} \exp\left(\frac{E_V - E_F}{kT}\right) \cdot \frac{\varepsilon'}{kT}. \quad (25)$$

When the uniaxial stress is $\bar{\sigma}$, the band shift ε' is (Hensel & Feher, 1963):

$$\varepsilon' = \frac{1}{3} D_u C_{44}^{-1} \bar{\sigma}, \quad (26)$$

where D_u is deformation potential constant, C_{44} is the corresponding elastic stiffness constant. Due to the different effective mass of heavy and light holes, the change in the corresponding hole concentrations can lead the tunneling current J_δ to vary, which is the principle of tunneling piezoresistive effect. The relative change of the equivalent tunneling resistivity is:

$$\frac{\Delta \rho_\delta}{\rho_\delta} = -\frac{\Delta J_\delta}{J_\delta} = -\frac{\Delta p_1 (J_{\delta 0})_1 + \Delta p_2 (J_{\delta 0})_2}{p_1 (J_{\delta 0})_1 + p_2 (J_{\delta 0})_2}. \quad (27)$$

Substituting Eqs. (20), (24) and (25) into Eq. (27), it yields:

$$\frac{\Delta\rho_\delta}{\rho_\delta}=\frac{1-\left(\frac{m_{d1}}{m_{d2}}\right)^{3/2}\cdot\frac{(J_{\delta 0})_1}{(J_{\delta 0})_2}}{1+\left(\frac{m_{d1}}{m_{d2}}\right)^{3/2}\cdot\frac{(J_{\delta 0})_1}{(J_{\delta 0})_2}}\cdot\frac{\varepsilon'}{kT}. \tag{28}$$

From Eqs. (21)-(23), it results in:

$$\frac{(J_{\delta 0})_1}{(J_{\delta 0})_2}=\frac{(c_1)_2\left\{\exp\left[(c_2)_1-\frac{a}{kT}\right]-\exp\left[2(c_2)_1\right]\right\}}{(c_1)_1\left\{\exp\left[(c_2)_2-\frac{a}{kT}\right]-\exp\left[2(c_2)_2\right]\right\}}, \tag{29}$$

where $(c_1)_j$ and $(c_2)_j$ can be determined by Eqs. (15) and (18), respectively. According to the experimental data (Mandurah, et al., 1981), the grain boundary width δ is set to be 1nm and the grain boundary barrier height $q\phi$ is about 0.6eV. Thus, for heavy holes, j=1, $(c_1)_1$ and $(c_2)_1$ are calculated to be -0.84 and -3.72, respectively; for light holes, j=2, $(c_1)_2$ and $(c_2)_2$ are calculated to be -0.94 and -1.46, respectively. In general, $qV_\delta \ll q\phi$, it can be obtained from Eq. (8) that $a \approx q\phi$. From Eq. (29) and Table 1, it yields:

$$\left(\frac{m_{d1}}{m_{d2}}\right)^{3/2}=\sqrt{\frac{m_{l1}m_{t1}^{\ 2}}{m_{l2}m_{t2}^{\ 2}}}=1.180, \tag{30}$$

$$\frac{(J_{\delta 0})_1}{(J_{\delta 0})_2}=1.22\times 10^{-2}. \tag{31}$$

Finally, using Eqs. (26), (28)-(31), the longitudinal PRC of grain boundary barriers along the <111> orientation is expressed as:

$$\pi_{\delta l}=\frac{\Delta\rho_\delta}{\rho_\delta\bar{\sigma}}=\frac{0.972}{3}\cdot D_u C_{44}^{\ -1}\cdot\frac{1}{k_0 T}. \tag{32}$$

Similarly, the transversal PRC along <111> orientation is:

$$\pi_{\delta t}=\frac{\Delta\rho_\delta}{\rho_\delta\bar{\sigma}}=\frac{-0.684}{3}\cdot D_u C_{44}^{\ -1}\cdot\frac{1}{k_0 T}. \tag{33}$$

From our previous research results, the longitudinal and transversal PRCs of p-type monocrystalline silicon (grain neutral regions) under a uniaxial stress $\bar{\sigma}$ applied along the <111> orientation can be expressed as follows, respectively (Liu, et al., 2004):

$$\pi_{gl}=\frac{0.695}{3}\cdot D_u C_{44}^{\ -1}\cdot\frac{1}{k_0 T}, \tag{34}$$

$$\pi_{gt} = -\frac{0.435}{3} \cdot D_u C_{44}^{-1} \cdot \frac{1}{k_0 T} . \quad (35)$$

Comparing Eqs. (32) and (33) with (34) and (35) correspondingly, it yields:

$$\pi_{\delta l} = 1.4\pi_{gl} , \quad (36)$$

$$\pi_{\delta t} = 1.6\pi_{gt} . \quad (37)$$

From Eqs. (36) and (37), it can be seen that the PRCs π_δ and π_g present a proportional relationship and the PRC π_δ is larger than π_g.

6.5 Piezoresistance coefficient of composite grain boundaries

From the above theoretical analysis, it can be seen that both the PRC of depletion region barriers and the PRC of grain boundary barriers are proportional to the PRC of grain neutral regions. Noticeably, according to Eqs. (4), (5), (36) and (37), the PRC of depletion region barriers π_d is lower than π_g, while the PRC of grain boundary barriers π_δ is higher than π_g. Therefore, the relationship between the PRC of composite grain boundaries π_b and the PRC of grain neutral regions π_g is dependent on the weights of the equivalent resistivities ρ_d (for depletion region barriers) and ρ_δ (for grain boundary barriers) in the equivalent resistivity ρ_b of composite grain boundaries. In this case, π_b can be expressed as:

$$\pi_b = \frac{\Delta\rho_b}{\rho_b \overline{\sigma}} = \frac{\rho_d}{\rho_b} \cdot \frac{\Delta\rho_d}{\rho_d \overline{\sigma}} + \frac{\rho_\delta}{\rho_b} \cdot \frac{\Delta\rho_\delta}{\rho_\delta \overline{\sigma}} = \frac{\rho_d}{\rho_b}\pi_d + \frac{\rho_\delta}{\rho_b}\pi_\delta , \quad (38)$$

where

$$\rho_b = \rho_d + \rho_\delta . \quad (39)$$

If the potential drops across depletion regions on the left and right hand sides of the grain boundary are denoted by V_L and V_R, respectively; then the potential drops on depletion region barriers and grain boundary barrier are V_L+V_R and V_δ, respectively. So, Eq. (38) can be expressed as follows:

$$\pi_b = \frac{V_L + V_R}{V_0}\pi_d + \frac{V_\delta}{V_0}\pi_\delta , \quad (40)$$

$$V_0 = V_\delta + V_L + V_R , \quad (41)$$

where V_0 is the potential drop over the composite grain boundary. Thus, it can be seen that determining the proportional relationship between V_L+V_R and V_δ is the key to solve out π_b. Because the polysilicon usually work under low current and low voltage bias, the condition of $V_L+V_R<4V_b$ can be always satisfied. Then, the relationship of V_L, V_R, V_b and V_δ can be obtained (Mandurah, et al., 1981):

$$2V_b^{1/2} = (V_b + V_R)^{1/2} + (V_b - V_L)^{1/2} , \quad (42)$$

$$V_\delta = \delta\left(\frac{qN_A}{2\varepsilon_s\varepsilon_0}\right)^{1/2}\left[(V_b+V_R)^{1/2}-(V_b-V_L)^{1/2}\right]. \tag{43}$$

According to the approximation of depletion region, it yields

$$V_b = \frac{qN_A W^2}{2\varepsilon_s\varepsilon_0}, \tag{44}$$

$$W = \frac{N_t}{2N_A}, \tag{45}$$

where N_A is the boron doping concentration, N_t is the trap density at grain boundary, ε_s and ε_0 are the relative and vacuum dielectric constants of silicon, respectively. In this paper, the trap density N_t is taken to be 1.0×10^{13} cm^{-2}. By calculating, the distribution of the voltage V_δ normalized to the voltage V_0 as a function of N_A is provided in inset of Fig. 14.

The experimental results indicate that the longitudinal piezoresistive sensitivity is twice larger than the transversal sensitivity. Hence, the following derivations are based on the longitudinal piezoresistive effect. Considering that the fundamental cubic piezoresistance coefficients π_{11}, π_{12} and π_{44} satisfy $\pi_{11}+2\pi_{12}<<2\pi_{44}$ for p-type single crystal silicon, the longitudinal piezoresistance coefficient π_{gl} can be taken to be $2\pi_{44}/3$. Therefore, combining Eqs. (4), (36), (40) and (41), the piezoresistance coefficient of composite grain boundary can be expressed as:

$$\pi_{bl} = (0.525 + 0.875\frac{V_\delta}{V_0})\pi_{gl} = (0.35 + 0.583\frac{V_\delta}{V_0})\pi_{44} \tag{46}$$

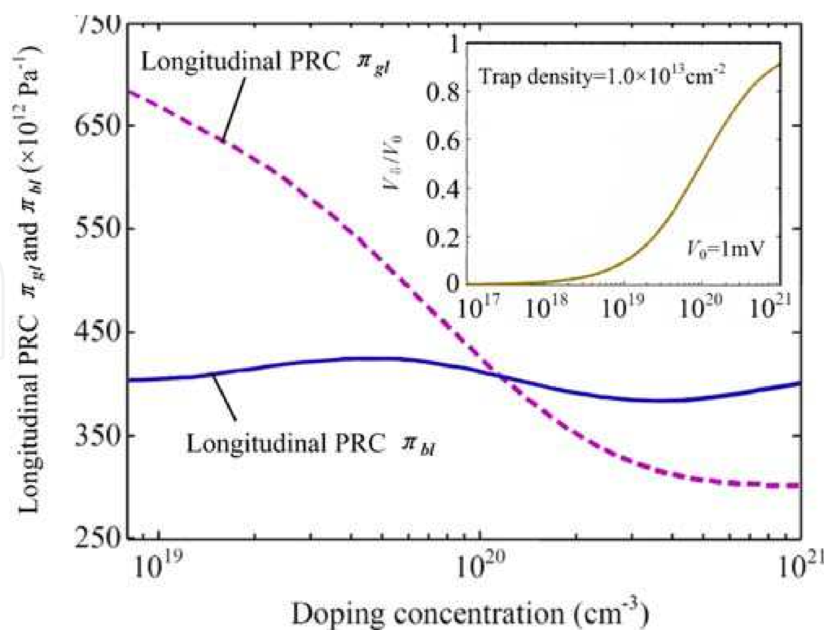

Fig. 14. Dependences of the longitudinal piezoresistance coefficients (π_{gl} and π_{bl}) and the potential drop ratio V_δ/V_0 on the doping concentration. The potential drop V_0 on composite grain boundary and the trap density at grain boundary is taken to be 1 mV and 1.0×10^{13} cm^{-2}.

In virtue of the dependences of the potential drop ratio V_δ/V_0 and π_{44} on the doping concentration (Tufte & Stelzer, 1963; Toriyama & Sugiyama, 2002; Shi, et al., 2009), the relational curves of longitudinal piezoresistance coefficients π_{gl} and π_{bl} on the doping concentration are obtained as shown in Fig. 14. Seen from the inset of Fig. 14, the potential drop ratio V_δ/V_0 increases sharply at high doping concentrations, therefore resulting in that the longitudinal PRC of composite grain boundary becomes much larger than that of grain neutral regions when V_δ/V_0 >0.543 (the doping concentration> 1.1×10^{20}cm^{-3}).

7. Experimental results and analyses

7.1 Magnetron sputtering samples

After high temperature annealing, micrograins are formed and the films transfer from the amorphous state to polycrystalline state. The dependence of the film resistivity on the annealing time is provided in Fig. 15. From Fig. 15, it can be seen that when the annealing time is 60 min, the film resistivity is the lowest. Noticeably, if the annealing is performed after the boron diffusion, the dopants are almost not activated and the corresponding resistivity is very high. It is likely due to that the most of boron dopants are captured by the dangling bonds, and the post-annealing is difficult to break the covalent bonds.

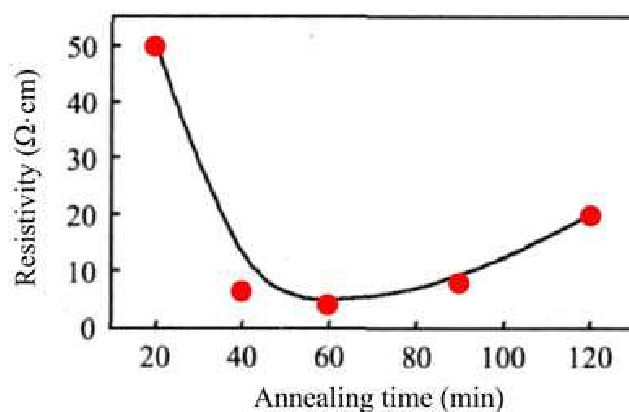

Fig. 15. Dependence of the resistivity of magnetron sputtering films on the annealing time

The measurement results show that the gauge factor of magnetron sputtering films is ranged from 10 to 80. The uniformity of experimental data is poor, so that this film preparation could not be suited for the fabrication of sensors. Once the crystallization of films is improved, the magnetron sputtering may be a favourable method of preparing polycrystalline silicon films.

7.2 LPCVD films with different thicknesses

The dependences of longitudinal gauge factor and grain size on film thickness are provided in Fig. 16. For PSCFs, the average value of gauge factor is between 20 and 25. It is due to that the larger grain size and better crystallinity reduce greatly the proportion of composite grain boundary resistivity to film resistivity, resulting in that the gauge factor depends on the piezoresistance coefficient of grain neutral regions. For PSNFs, the average gauge factor is enhanced to be 32~34. Due to the reduction of film thickness, the film crystallinity and the grain size are both diminished clearly; at the same time, the grain boundary width and the trap density at grain boundaries increase correspondingly. Therefore, the proportion of

composite grain boundary resistivity to film resistivity is improved further. In this case, the gauge factor depends on the piezoresistance coefficient of composite grain boundary. According to the above tunneling piezoresistive theory, when the trap density at grain boundaries is not too high, the piezoresistance coefficient of composite grain boundary is larger than that of grain neutral regions at high doping levels. Hence, the PSNFs exhibit the enhanced piezoresistive sensitivity (about 50%), compared with the PSCFs. The intervenient films are ascribed to the transition type.

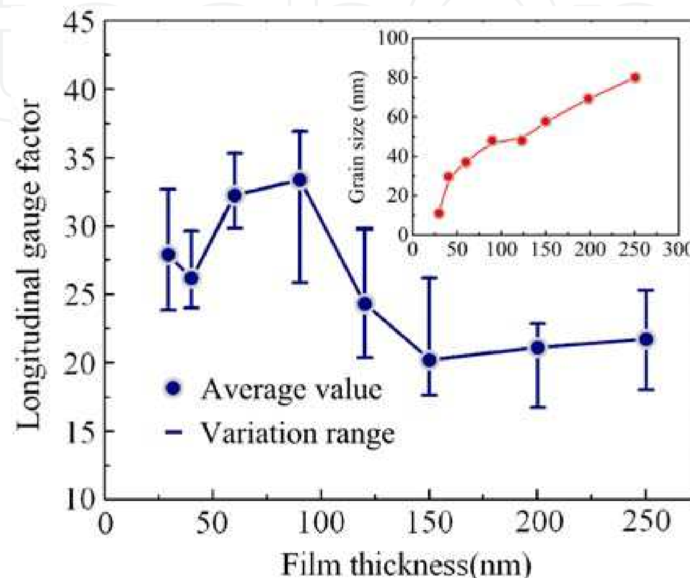

Fig. 16. Longitudinal gauge factor and grain size of polysilicon thin films with different thicknesses.

When the film thickness is further reduced (thinner than 50 nm), the film crystallinity and the grain size are diminished greatly, thereby resulting in the increase of trap density at grain boundaries. At the same doping level, this makes more carriers captured by traps at grain boundaries and broadens the width of DRBs beside the grain boundary. When the current flows through the composite grain boundary, the potential drop on broadened DRBs increases. According to Eqs. (40) and (41), it increases the proportion of DRB piezoresistance coefficient to composite grain boundary piezoresistance coefficient. Based on the tunneling piezoresistive theory, the piezoresistance coefficient of DRBs is much smaller than that of grain neutral regions and grain boundary barriers. Consequently, the composite grain boundary piezoresistance coefficient of NL-PSTFs is reduced compared with the PSNFs. Although the increase in trap density improves the proportion of the composite grain boundaries of NL-PSTFs, the decrease of the composite grain boundary piezoresistance coefficient makes the longitudinal gauge factor of NL-PSTFs smaller than that of PSNFs. Additionally, the NL-PSTFs is the transition type towards the nanocrystalline silicon. Due to the high gauge factor of nanocrystalline silicon (He, et al., 1996), the gauge factor of NL-PSTFs increases slightly with the reduction of film thickness.

7.3 LPCVD films with different doping concentrations

The relationship between the longitudinal gauge factor of 80 nm-thick PSNFs and doping concentration is shown in Fig. 17. It can be seen from Fig. 17 that the gauge factor reaches the maximum as the doping concentration is about 4×10^{19} cm^{-3}; however, when the doping

concentration is higher than 2×10^{20} cm^{-3}, the gauge factor increases again with the increase of doping concentration. This exceptional increase of gauge factor has not been observed in polysilicon thicker films and can not be explained reasonably by the existing piezoresistive theory. Here, the phenomenon is analyzed based on the tunneling piezoresistive theory.
The longitudinal gauge factor of PSNFs could be expressed as the weighted superposition of gauge factors of grain neutral regions and composite grain boundaries, and the weight factors are the products of the resistivity ratios and width ratios of grain neutral regions and composite grain boundaries to films, respectively. Thus, the longitudinal gauge factor of PSNFs can be given by:

$$GF_l = \frac{L-(2w+\delta)}{L}\cdot\frac{\rho_g}{\rho}GF_{gl} + \left[1-\frac{L-(2w+\delta)}{L}\cdot\frac{\rho_g}{\rho}\right]GF_{bl} \tag{47}$$

where ρ_g and ρ are the resistivity of grain neutral regions and the film resistivity, respectively; L is the grain size; GF_{gl} and GF_{bl} are the longitudinal gauge factors of grain neutral regions and composite grain boundaries, respectively.

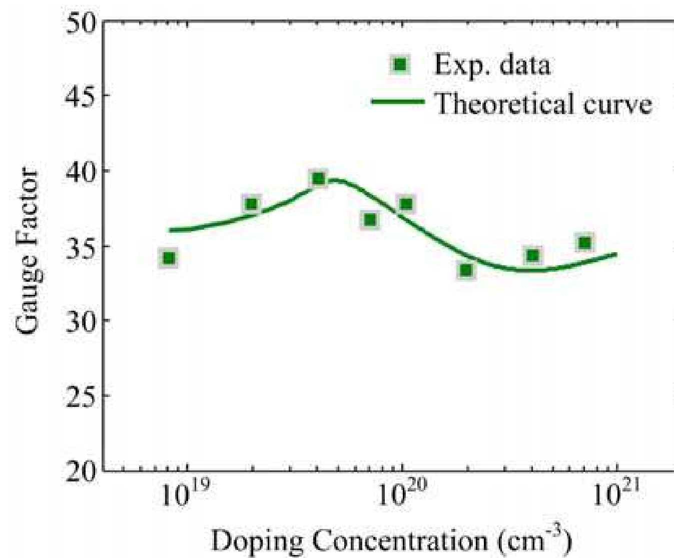

Fig. 17. Experiment data and theoretical curve of the longitudinal gauge factor of the PSNFs with different doping concentrations

Due to the random orientation of PSNFs, the gauge factors GF_l, GF_{gl} and GF_{bl} should be substituted by the average gauge factors $<GF_l>$, $<GF_{gl}>$ and $<GF_{bl}>$ derived along the all orientations. Based on the method presented by Schubert (Schubert, et al., 1987), the proportion factor of the average gauge factors ($<GF_{gl}>$ and $<GF_{bl}>$) with random grain orientations and the gauge factors ($GF_{gl,<111>}$ and $GF_{bl,<111>}$) along the $<111>$ orientation was calculated to be 0.537. Therefore, the average gauge factors can be expressed as:

$$<GF_{gl}>=0.537GF_{gl,<111>} = 0.537\cdot(1+2\upsilon+f_Y\cdot Y_{Si<111>}\pi_{gl,<111>}) \tag{48}$$

$$<GF_{bl}>=0.537GF_{bl,<111>} = 0.537\cdot(1+2\upsilon+f_Y\cdot Y_{Si<111>}\pi_{bl,<111>}) \tag{49}$$

where υ is Poisson's ratio and taken to be 0.25, $Y_{Si<111>}$ is Young's modulus of single-crystal silicon along $<111>$ orientation and taken to be 1.87×10^{20} Pa, f_Y is a correction factor and

taken to be 0.85, $\pi_{gl,<111>}$ and $\pi_{bl,<111>}$ are the piezoresistance coefficients of grain neutral regions and composite grain boundaries along the <111> orientation, respectively. The introduction of the correction factor f_Y is due to that the Young's modulus of polysilicon is lower than that of single-crystal silicon (Greek, et al., 1999; Yi & Kim, 1999).

According to Eq. (47), in order to figure out the relationship between the longitudinal gauge factor and doping concentration, it is necessary to determine the resistivity ratio ρ_g/ρ. Generally, when calculating the gauge factor, the resistivity of grain neutral regions ρ_g is taken to be the value of monocrystalline silicon (Schubert, et al., 1987; Mosser, et al., 1991), and the resistivity of polysilicon ρ is taken to be the actual measured value. For the samples with different doping concentrations, the fitting dependence of ρ on N_A at room temperature is:

$$\rho = 15.651e^{-1.73\times10^{-19}N_A} + 0.014 \ (\Omega\ \text{cm}) \tag{50}$$

In semiconductor physics, the resistivity ρ_g at room temperature can be expressed as

$$\rho_g = a_s N_A^{-1} + a_i \tag{51}$$

where a_s and a_i are the constants determined by the scattering probability resulted from the acoustic phonons and impurity scattering, respectively. According to the relational curve of the resistivity of p-type monocrystalline silicon versus doping concentration, in the doping concentration range of 5×10^{18}~10^{21} cm^{-3}, by fitting in the function form of Eq. (51), the relationship between ρ_g and N_A at room temperature is

$$\rho_g = 6.8741\times10^{16} N_A^{-1} + 2\times10^{-3} \ (\Omega\ \text{cm}) \tag{52}$$

Although the grain neutral regions possess monocrystal structure, the defect density is very high and increases with the grain size reducing. Therefore, it is necessary to take the scattering process of lattice defects into consideration when calculating the resistivity. If the defect density is independent of doping concentration, a modifying factor a_d determined by defect density can be introduced, thus Eq. (52) can be modified as

$$\rho_g = (6.8741\times10^{16} + a_d) N_A^{-1} + 2\times10^{-3} \ \ (\Omega\ \text{cm}) \tag{53}$$

For the PSNFs mentioned here, the value of a_d is 2×10^{16} Ω cm^{-2}. Here, the scattering process of lattice defects is equivalent to the ionized impurity scattering at the doping concentration of 10^{19} cm^{-3}. This is comprehensible for the PSNFs (the thickness is 80 nm and the average grain size is 27 nm). When it is assumed that 1% of the bonds on the grain surface are dangling bonds and these dangling bonds are regarded as defects, the defect density is at the level of 10^{19} cm^{-3}. Using Eqs. (47)–(50) and (53) obtained from the above analysis and combining the dependences of piezoresistance coefficients π_{gl} and π_{bl} on N_A, the theoretical curve of gauge factor versus doping concentration for PSNFs was gained in Fig. 17. Thus, it was seen that the calculating results of tunnelling piezoresistive model were greatly in agreement with the experiment data.

7.4 LPCVD films with different deposition temperatures

Fig. 18 provides the resistivity of highly boron doped PSNFs versus deposition temperature. It can be seen that the resistivity changes from 1.54×10^{-1} to 4.9×10^{-3} Ω·cm with elevating deposition temperature. Considering the experiment results that the grain size increases

with raising deposition temperature, it indicates that the weight of the resistivity of composite grain boundaries ρ_b in the resistivity of PSNFs ρ is reduced by increasing deposition temperature. Because ρ_b is dependent on the resistivity of grain boundary barriers ρ_δ and the resistivity of depletion region barriers ρ_d (i.e., $\rho_b = \rho_\delta + \rho_d$), the elevation of deposition temperature might reduce either of ρ_δ and ρ_d. According to the SEM and XRD results, there are more amorphous contents in RC PSNFs (560~600°C samples) than in DC PSNFs (620~670°C samples). The existence of amorphous phases at grain boundaries could increase the resistivity ρ_δ. On the other hand, the high doping concentration narrows the width of depletion region barriers to a few angstroms, so that the contribution of ρ_d to ρ_b could be neglected. Therefore, at high doping concentration, the resistivity of composite grain boundaries ρ_b is dependent on the resistivity of grain boundary barriers ρ_δ, and the reduction of amorphous contents at grain boundaries caused by elevating deposition temperature is responsible for the falloff of the film resistivity ρ. However, the resistivity of 620°C samples is slightly higher than that of 600°C ones. It is likely due to the recrystallization of 600°C samples after the pre-annealing at 950°C.

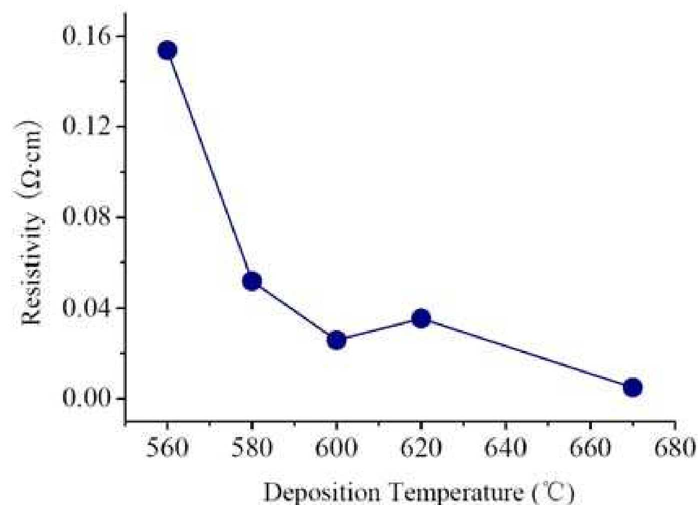

Fig. 18. Resistivity of boron doped PSNFs versus deposition temperature

The dependences of the resistance change $\Delta R/R_0$ in longitudinal and transversal piezoresistors on the strain ε with different deposition temperatures are shown in Figs. 19(a) and (b), respectively. Obviously, the longitudinal and transversal piezoresistances vary linearly with the strain. From the insets of Figs. 19(a) and (b), it can be seen that RC PSNFs and DC PSNFs exhibit different piezoresistive properties. And the critical deposition temperature differentiating RC PSNFs and DC PSNFs is around 605°C. The samples deposited below this critical temperature present amorphous appearance mixed with polycrystals, while the samples above this value present better polysilicon appearance. This critical value is consistent with the reported result (French & Evens, 1989).

For the longitudinal piezoresistive sensitivity, it can be seen in Fig. 19(a) that the gauge factors of RC or DC PSNFs decrease with elevating deposition temperature. As discussed above, the amorphous contents at grain boundaries are reduced by raising deposition temperature. For RC PSNFs, when the deposition temperature is lowered, the crystallinity of samples is aggravated and there are more amorphous phases existing at grain boundaries. The increase of amorphous phases raises the resistivity ρ_δ. Moreover, the deficient crystallinity increases the width of grain boundary barriers δ and further increases the weight of ρ_b in the film resistivity

ρ. According to the existing piezoresistive model, the PRCs of DRBs (π_d) and grain boundary barriers (π_δ) are lower than that of grain neutral regions π_g. Thus, it implies that the piezoresistive sensitivity of PSNFs with more amorphous contents and smaller grain size should be much lower. However, it is obvious that the deduction is inconsistent with the experiment results. Based on the tunneling piezoresistive theory presented here, the longitudinal PRC of composite grain boundaries π_{bl} is much larger than that of grain neutral regions π_{gl} at high doping concentration. As a result of lowering deposition temperature, both the resistivity ρ_b and the weight of ρ_b in the film resistivity ρ increase. It enhances the contribution of the PRC π_{bl} on the piezoresistive sensitivity, thereby increasing longitudinal gauge factors. For DC PSNFs, the XRD analysis indicates that there are more amorphous phases in the 670°C samples than in the 620°C ones, which is likely due to the <110> preferred growth aggravating disordered states of grain boundaries. It makes the resistivity ρ_δ of 670°C samples higher than 620°C samples. However, the SEM results show that the grain size of 670°C samples is ~70nm and much larger than that of 620°C ones. This reduces severely the weight of the resistivity ρ_b in the film resistivity ρ and weakens the contribution of the PRC π_{bl} on the piezoresistive sensitivity. Therefore, the longitudinal gauge factor of 670°C samples with larger grains is much lower than that of 620°C ones.

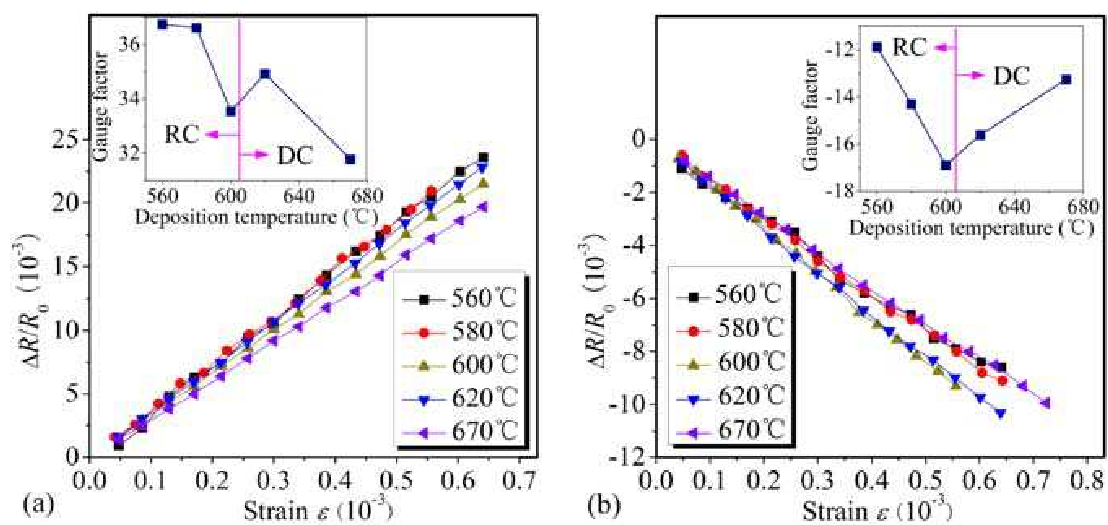

Fig. 19. (a) Dependences of the resistance change $\Delta R/R_0$ in longitudinal piezoresistors on strain ε with different deposition temperatures, and the longitudinal gauge factor vs. deposition temperature. (b) Dependences of $\Delta R/R_0$ in transversal piezoresistors on strain ε with different deposition temperatures, and the transversal gauge factor vs. deposition temperature.

For the transversal piezoresistive sensitivity, the inset of Fig. 19(b) shows that the magnitude of the transversal gauge factor in DC PSNFs increases with lowering deposition temperature, similar to the longitudinal gauge factor dependence; while the magnitude of the transversal gauge factor in RC PSNFs falls off drastically with lowering deposition temperature. Comparing the insets of Figs. 19(a) and (b), it can be seen that the longitudinal gauge factor of DC PSNFs is about twice larger than the transversal one. However, the longitudinal and transversal gauge factors of RC PSNFs do not satisfy the above proportional relation. On the contrary, the transversal gauge factor of RC PSNFs decreases from 1/2 to 1/3 of the longitudinal one with lowering deposition temperature, which might be due to the degradation of transversal piezoresistive effect in amorphous silicon.

It is noteworthy that the stress-induced modulation of surface depletion region width in silicon nanowires (He &Yang, 2006) is not fit for the explanation of enhanced piezoresistive effect in PSNFs. For silicon nanowires, the surface depletion regions are parallel to the direction of carrier transport, and the change in surface potential barrier caused by stress only influences the conducting channel width of carriers along silicon nanowires. However, for PSNFs, the depletion regions are perpendicular to the direction of carrier transport and the carriers have to traverse them by thermionic emission or tunneling. Moreover, the depletion region width is reduced greatly at high doping concentration and can be neglected. So the tunneling effect of carriers becomes dominant.

8. PSNF-based pressure sensor

Fig. 20 provides the photo of a PSNF-based pressure sensor. In Fig. 20, there are 4 sets of half Wheatstone bridge; precise matching of piezoresistors can be obtained by selecting proper half bridge. Some main performance characteristics of the PSNF-based pressure sensor are listed in Table 2. It can be seen that the PSNF-based pressure sensor possesses favourable sensitivity and temperature stability.

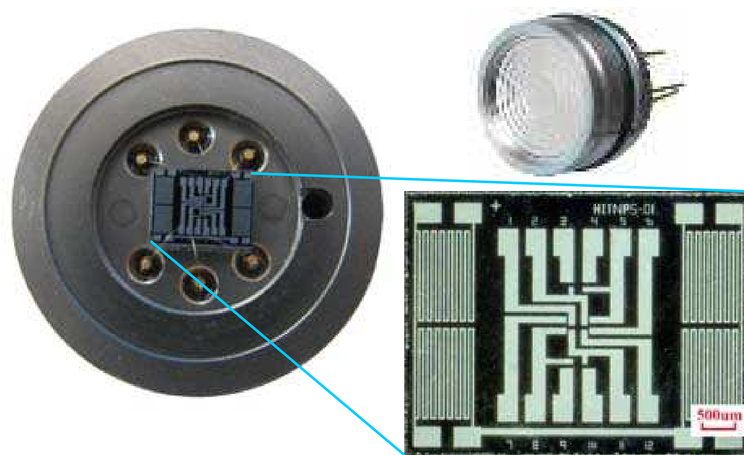

Fig. 20. Photos of PSNF-based pressure sensor chip and packaging

Parameter	Value	
Working temperature (°C)	25	200
Sensitivity (mV/V/MPa)	22.23	18.27
Full scale output (mV)	66.38	54.82
Offset (mV)	9.63	9.49
Temperature coefficient of sensitivity (%/°C)	-0.098	-0.098
Temperature coefficient of offset (%/°C)	-0.017	-0.017
Linearity (%FS)	0.06	0.38
Hysteresis (%FS)	0.49	0.93
Repeatability (%FS)	1.08	2.07

Table 2. Performance characteristics of the PSNF-based pressure sensor

9. Summary

Our research group has been spending a great effort on the investigation of polycrystalline silicon-based sensors. Through the alteration of technological conditions, the enhanced piezoresistance effect of heavily doped polycrystalline silicon nano thin films was discovered, and this characteristic could be used in the design and fabrication of piezoresistive sensors with miniature volume, high sensitivity and wide working temperature range. In the experiments, the influences of film thickness, doping concentration and deposition temperature on the piezoresistive properties of polycrystalline silicon films were studied. The results indicate that the optimal technological parameters are: the thickness of polycrystalline silicon film is in the range of 80-90 nm; the doping concentration is $2\text{-}3\times10^{20}$ cm^{-3}; the deposition temperature is set to be 620 °C. Additionally, in order to explain reasonably the unique piezoresistive phenomenon, the tunnelling piezoresistive model was established. In this model, the contribution of grain boundaries to the piezoresistive effect is taken into consideration. By calculation and derivation, it is proved that the piezoresistance coefficient of composite grain boundaries is much higher than that of grain neutral regions at high doping levels. The experimental data and the theoretical results gain a good agreement. Finally, the PSNF-based pressure sensor was fabricated successfully. The test results show that the sensor provides high sensitivity and very low temperature coefficients. Therefore, it can be concluded that the polycrystalline silicon nano thin films could be potential for the application of MEMS-based piezoresistive sensors.

10. References

Erskine, J.C. (1983). Polycrystalline silicon-on-metal strain gauge transducers. *IEEE Trans. Electron Dev.*, Vol. ED-30, 796-801, 0018-9383

French, P.J.; Evens, A.G.R. (1989). Piezoresistance in polysilicon and its applications to strain gauges. *Solid-State Electron*, Vol. 32, 1-10, 0038-1101

Germer, W.; Tödt, W. (1983). Low-cost pressure/force transducer with silicon thin film strain gauges. *Sens. Actuators*, Vol. 4, 183-189, 0250-6874

Greek, S.; Ericson, F.; Johansson, S.; Furtsch, M.; Rump, A. (1999). Mechanical characterization of thick polysilicon films: Young's modulus and fracture strength evaluated with microstructures. *J. Micromech. Microeng.*, Vol. 9, 245-251, 0960-1317

Gridchin, V.A.; Lubimsky, V.M.; Sarina, M.P. (1995). Piezoresistive properties of polysilicon films. *Sens. Actuators A*, Vol. 49, 67-72, 0924-4247

He, R.; Yang, P. (2006). Giant piezoresistance effect in silicon nanowires. *Nature Nanotech.*, Vol. 1, 42-46, 1748-3387

He, Y.L.; Liu, H.; Yu, M.B.; Yu, X.M. (1996). The structure characteristics and piezo-resistance effect in hydrogenated nanocrystalline silicon films. *Nanostructured Materials*, Vol. 7, 769-777, 0965-9773

Hensel, J.C.; Feher, G. (1963). Cyclotron resonance experiments in uniaxially stressed silicon: valence band inverse mass parameters and deformation potentials. *Phys. Rev.*, Vol. 129, 1041-1062, 0031-899X

Herring, C. (1955). Transport properties of a many-valley semiconductor. *Bell Syst. Tech. J.*, Vol. 34, 237-290, 0030-4018

Jaffe, J.M. (1983). Monolithic polycrystalline silicon pressure transducer. *IEEE Trans. Electron. Dev.*, Vol. ED-30, 420-421, 0018-9383

Kamins, T.I. (1971). Hall mobility in chemically deposited polycrystalline silicon. *J. Appl. Phys.*, Vol. 42, 4357-4365, 0021-8979

Le Berre, M.; Kleimann, P.; Semmache, B. ; Barbier, D. ; Pinard, P. (1996). Electrical and piezoresistive characterization of boron-doped LPCVD polycrystalline silicon under rapid thermal annealing. *Sens. Actuators A*, Vol. 54, 700-703, 0924-4247

Liu, X.W.; Huo, M.X.; Chen, W.P.; Wang, D.H.; Zhang, Y. (2004). Theoretical research on piezoresistive coefficients of polysilicon films. *Chin. J. Semiconduct.*, Vol. 25, 292-296, 0253-4177

Luder, E. (1986). Polycrystalline silicon-based sensors. *Sens. Actucators*, Vol. 10, 9-23, 0250-6874

Malhaire, C.; Barbier, D. (2003). Design of a polysilicon-on-insulator pressure sensor with original polysilicon layout for harsh environment. *Thin Solid Films*, Vol. 427, 362-366, 0040-6090

Mandurah, M.M.; Saraswat, K.C.; Kamins, T.I. (1981). A model for conduction in polycrystalline silicon-Part I: theory. *IEEE Trans. Electron Dev.*, Vol. ED-28, 1163-1171, 0018-9383

Mikoshiba, H. (1981). Stree-sensitive properties of silicon-gate MOS devices. *Solid-State Electron*, Vol. 24, 221-232, 0038-1101

Mosser, V.; Suski, J.; Goss, J.; Obermeier, E. (1991). Piezoresistive pressure sensors based on polycrystalline silicon. *Sens. Actuators A*, Vol. 28, 113-131, 0924-4247

Murphy, E.L.; Good, R.H. (1956). Thermionic emission, field emission and the transition region. *Phys. Rev.*, Vol. 102, 1464-1469, 0031-899X

Onuma, Y.; Sekiya, K. (1974). Piezoresistive properties of polycrystalline silicon thin film. *Jpn. J. Appl. Phys.*, Vol. 11, 420-421, 0021-4922

Rowe, A.C.H. (2008). Silicon nanowires feel the pinch. *Nature Nanotech.*, Vol. 3, 311-312, 1748-3387

Rowe, A.C.H.; Donoso-Barrera, A.; Renner, Ch.; Arsott, S. (2008). Giant room-temperature piezoresistance in a metal-silicon hybrid structure. *Phys. Rev. Lett.*, Vol. 100, 145501-1-4, 0031-9007

Schubert, D.; Jenschke, W.; Uhlig, T.; Schmidt, F.M. (1987). Piezoresistive properties of polycrystalline and crystalline silicon films. *Sens. Actuators*, Vol. 11, 145-155, 0250-6874

Shi, C.-Z.; Liu, X.-W.; Chuai, R.-Y. (2009). Piezoresistive sensitivity, linearity and resistance time drift of polysilicon nanofilms with different deposition temperatures. *Sensors*, Vol. 9, No. 2, 1141-1166, 1424-8220

Smith, C.S. (1954). Piezoresistance effect in germanium and silicon. *Phys. Rev.*, Vol. 94, 42-49, 0031-899X

Taniguchi, M.; Hirose, M.; Osaka, Y. (1978). Substitutional doping of chemically vapor-deposited amorphous silicon. *J. Cryst. Growth*, Vol. 45, 126-129, 0022-0248

Toriyama, T.; Sugiyama, S. (2002). Analysis of piezoresistance in p-type silicon for mechanical sensors. *J. Microelectronmech. Syst.*, Vol. 11, 598-604, 1057-7157

Tufte, O.N.; Stelzer, E.L. (1963). Piezoresistive properties of silicon diffused layers. *J. Appl. Phys.*, Vol. 34, 313-318, 0021-8979

Wang, M.X.; Meng, Z.G.; Zohar, Y.; Wong, M. (2001). Metal-induced laterally crystallized polycrystalline silicon for integrated sensor applications. *IEEE Trans. Electron. Dev.*, Vol. 48, 794-800, 0018-9383

Yi, T.-C.; Kim, C. -J. (1999). Measurement of mechanical properties for MEMS materials. *Meas. Sci. Technol.*, Vol. 10, 706-716, 0957-0233

Zhao, Z.X.; Cui, R.Q.; Meng, F.Y.; Zhao, B.C.; Yu, H.C.; Zhou, Z.B. (2004). Nanocrystalline silicon thin films prepared by RF sputtering at low temperature and heterojunction solar cell. *Materials Letters*, Vol. 58, 3963-3966, 0167-577X

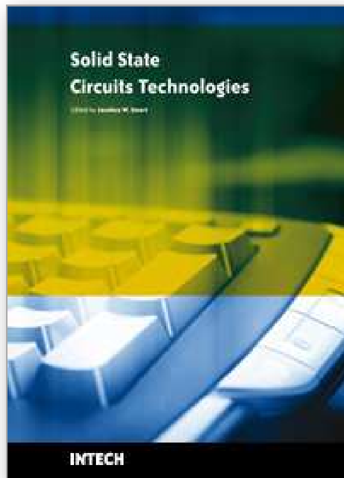

Solid State Circuits Technologies
Edited by Jacobus W. Swart

ISBN 978-953-307-045-2
Hard cover, 462 pages
Publisher InTech
Published online 01, January, 2010
Published in print edition January, 2010

The evolution of solid-state circuit technology has a long history within a relatively short period of time. This technology has lead to the modern information society that connects us and tools, a large market, and many types of products and applications. The solid-state circuit technology continuously evolves via breakthroughs and improvements every year. This book is devoted to review and present novel approaches for some of the main issues involved in this exciting and vigorous technology. The book is composed of 22 chapters, written by authors coming from 30 different institutions located in 12 different countries throughout the Americas, Asia and Europe. Thus, reflecting the wide international contribution to the book. The broad range of subjects presented in the book offers a general overview of the main issues in modern solid-state circuit technology. Furthermore, the book offers an in depth analysis on specific subjects for specialists. We believe the book is of great scientific and educational value for many readers. I am profoundly indebted to the support provided by all of those involved in the work. First and foremost I would like to acknowledge and thank the authors who worked hard and generously agreed to share their results and knowledge. Second I would like to express my gratitude to the Intech team that invited me to edit the book and give me their full support and a fruitful experience while working together to combine this book.

How to reference
In order to correctly reference this scholarly work, feel free to copy and paste the following:

Xiaowei Liu, Changzhi Shi and Rongyan Chuai (2010). Polycrystalline Silicon Piezoresistive Nano Thin Film Technology, Solid State Circuits Technologies, Jacobus W. Swart (Ed.), ISBN: 978-953-307-045-2, InTech, Available from: http://www.intechopen.com/books/solid-state-circuits-technologies/polycrystalline-silicon-piezoresistive-nano-thin-film-technology

INTECH
open science | open minds

InTech Europe
University Campus STeP Ri
Slavka Krautzeka 83/A
51000 Rijeka, Croatia
Phone: +385 (51) 770 447
Fax: +385 (51) 686 166
www.intechopen.com

InTech China
Unit 405, Office Block, Hotel Equatorial Shanghai
No.65, Yan An Road (West), Shanghai, 200040, China
中国上海市延安西路65号上海国际贵都大饭店办公楼405单元
Phone: +86-21-62489820
Fax: +86-21-62489821

© 2010 The Author(s). Licensee IntechOpen. This chapter is distributed under the terms of the Creative Commons Attribution-NonCommercial-ShareAlike-3.0 License, which permits use, distribution and reproduction for non-commercial purposes, provided the original is properly cited and derivative works building on this content are distributed under the same license.